Chapter 6
Modeling Magnetospheric Fields in the Jupiter System

Joachim Saur, Emmanuel Chané, and Oliver Hartkorn

Abstract The various processes which generate magnetic fields within the Jupiter system are exemplary for a large class of similar processes occurring at other planets in the solar system, but also around extrasolar planets. Jupiter's large internal dynamo magnetic field generates a gigantic magnetosphere, which in contrast to Earth's magnetosphere is strongly rotational driven and possesses large plasma sources located deeply within the magnetosphere. The combination of the latter two effects is the primary reason for Jupiter's main auroral ovals. Jupiter's moon Ganymede is the only known moon with an intrinsic dynamo magnetic field, which generates a mini-magnetosphere located within Jupiter's larger magnetosphere including two auroral ovals. Ganymede's mini-magnetosphere is qualitatively different compared the one from Jupiter. It possesses no bow shock but develops pronounced Alfvén wings similar to most of the extrasolar planets which orbit their host stars within 0.1 AU. New numerical models of Jupiter's and Ganymede's magnetospheres presented here provide quantitative insight into these magnetospheres and the processes which maintain them. Jupiter's magnetospheric field is time-variable on various scales. At the locations of Jupiter's moons time-periodic magnetic fields induce secondary magnetic fields in electrically conductive layers such as subsurface oceans. In the case of Ganymede, these secondary magnetic fields influence the oscillation of the location of its auroral ovals. Based on dedicated Hubble Space Telescope observations, an analysis of the amplitudes of the auroral oscillations provides evidence that Ganymede harbors a subsurface ocean. Callisto in contrast does not possess a mini-magnetosphere, but still shows a perturbed magnetic field environment generated by induction within an electrically conductive layer and due to the plasma interactions with its atmosphere. Callisto's ionosphere and atmospheric UV emission is different compared to the other Galilean satellites

J. Saur (✉) • O. Hartkorn
Institute of Geophysics and Meteorology, University of Cologne, Albertus Magnus Platz, 50937 Cologne, Germany
e-mail: saur@geo.uni-koeln.de; hartkorn@geo.uni-koeln.de

E. Chané
Centre for Mathematical Plasma Astrophysics, KU Leuven, Celestijnenlaan 200B, 3001 Leuven, Belgium
e-mail: emmanuel.chane@kuleuven.be

H. Lühr et al. (eds.), *Magnetic Fields in the Solar System*, Astrophysics and Space Science Library 448, DOI 10.1007/978-3-319-64292-5_6

as it has primarily been generated by solar photons compared to magnetospheric electrons. At Callisto a fluid-kinetic model of the ionospheric electron distribution provides constraints on Callisto's oxygen atmosphere.

6.1 Introduction

The plasma interactions in and around Jupiter's magnetosphere and around Jupiter's moons are so rich in various phenomena that a huge class of interactions occurring at other planetary bodies in the solar system and at extrasolar planets are represented by the processes in the Jupiter system. In this chapter, we will present results of new models of the interaction of Jupiter's magnetosphere with the solar wind and interactions at the Galilean moons with particular focus on Ganymede and Callisto.

Jupiter is the largest planet with the largest magnetic moment in the solar system. Its interaction with the solar wind generates a planetary magnetosphere, which would appear to an observer on Earth larger compared to how the sun appears to us in the sky if Jupiter's magnetosphere could be seen with the naked eye. The four large Galilean moons, Io, Europa, Ganymede, and Callisto are all located within Jupiter's gigantic magnetosphere, and are subject to the interactions generated by Jupiter's magnetospheric plasma. The interaction at these moons differs due to the different properties of the moons. For example, Ganymede possesses an internal dynamo magnetic field which leads to its own mini-magnetosphere within Jupiter's magnetosphere. The other moons in contrast only possess weak internal magnetic fields generated by electromagnetic induction in electrically conductive layers.

In the next Sect. 6.2 we categorize the plasma interactions in Jupiter's magnetosphere based on various parameters. With this background we then describe the interaction of the solar wind with Jupiter in order to better understand Jupiter's magnetosphere (see Sect. 6.3). In the subsequent Sect. 6.4 we investigate time-variable effects in Jupiter's magnetosphere, which can be subdivided into periodic and non-periodic variabilities. The associated time-variable magnetic fields induce secondary magnetic fields in electrically conductive layers within the moons. Measurements of these induced fields are diagnostic of internal layers, such as saline subsurface oceans. The plasma of Jupiter's magnetosphere interacts with the atmospheres and ionospheres and the interior of the moons. Properties of this interaction, the formation of the ionospheres and the generation of related magnetic fields will be discussed for Ganymede and Callisto in Sects. 6.5 and 6.7. A novel technique to search for induced magnetic fields from a subsurface ocean within Ganymede based on Hubble Space Telescope observations of its auroral ovals is described in Sect. 6.6.

6.2 Characterization and Description of the Interaction

The plasma interactions of flows past planetary bodies can be characterized into different classes, which we discuss in the next subsection. Afterwards we provide an overview of the magnetohydrodynamic (MHD) approach to describe these interactions.

6.2.1 Overview of the Interaction

The interaction of a planetary body with its surrounding plasma is controlled by two factors: (1) the properties of the plasma flowing past the planetary object (discussed in Sect. 6.2.1.1) and (2) the properties of the planetary body itself (discussed in Sect. 6.2.1.2). Other overviews of the plasma interaction at Jupiter and its moons can be found, e.g., in Neubauer (1998), Kivelson et al. (2004) or Krupp et al. (2004).

6.2.1.1 Mach Numbers and Nature of Interaction

A key property which controls the interaction is the ratio of the relative bulk flow velocity v_0 between the plasma and the planetary object compared to the group velocities of the three magnetohydrodynamic waves. These ratios are called the fast Mach number M_f, the Alfvén Mach number M_A, and the slow mode Mach number M_s and refer to the ratios of the flow velocity to the fast magneto-sonic mode, the Alfvén mode, and the slow magneto-sonic mode, respectively (e.g., Baumjohann and Treumann 1996). If the fast mode is larger than 1, a bow shock forms ahead of the object for nearly all object classes. Exceptions are inert moons, i.e., without atmosphere and intrinsic magnetic fields. For $M_f < 1$, the bow shock disappears which is always the case if $M_A < 1$, i.e., if the flow is sub-Alfvénic.

The interaction of all planets in the solar system with the solar wind is such that under average conditions the solar wind flow is super-fast, i.e., $M_f > 1$ and all planets are surrounded by a bow shock. Only exceptionally, i.e., approximately once every 2 years, the plasma density in the solar wind is so low that the resultant Alfvén velocity $v_A = B/\sqrt{\mu_0 \rho}$ is faster than the solar wind velocity with the mass density ρ and the magnetic permeability of free space μ_0. In this case, the Earth loses its bow shock (Chané et al. 2012, 2015). This transition has however never been observed for Jupiter. In the case of Jupiter's moons, which are embedded within Jupiter's magnetosphere, the relative flow velocity is smaller than the Alfvén velocity and thus no bow shock forms, but so-called Alfvén wings develop (Neubauer 1980; Goertz 1980; Southwood et al. 1980). Alfvén wings are standing Alfvén waves in the restframe of the moons. The Alfvén waves are generated because the obstacle slows the flow of the magnetized plasma in its vicinity and generates stresses in the magnetic field. The Alfvén wings can be described as "tubes" in direction parallel

and anti-parallel to the magnetic field but with additional tilts by an angle $\Theta_A \approx \tan^{-1} M_A$ with respect to the magnetic field (Neubauer 1980).

Extrasolar planets are observed to orbit their host stars at a wide range of radial distances from ≈0.01 to 1000 AU. Because the stellar plasma properties are expected to strongly evolve as a function of distance similar to the solar wind properties of the sun (e.g., Parker 1958; Preusse et al. 2006; Lanza 2008), the plasma conditions around the observed extrasolar planets are expected to vary strongly. In Fig. 6.1, we show the expected Alfvén Mach number M_A near the 850 extrasolar planets known until 2013 (from Saur et al. 2013). The Mach number is calculated based on measured and estimated properties of the host stars and by applying the Parker (1958) model for the radial evolution of the stellar winds. Figure 6.1 shows that extrasolar planets at orbital distances approximately less than 0.1 AU are typically subject to sub-Alfvénic conditions. At these bodies no bows shock but Alfvén wings form. In case such an extrasolar planet possesses a dynamo magnetic fields as expected (Christensen et al. 2009), then the solar system analogue of these extrasolar planet is Ganymede. In case they do not possess a dynamo field, their interaction is qualitatively similar to Io, Europa, and Callisto. This comparison only relates to the sub-Alfvénic character of the interaction and the principal nature of the obstacle. The atmospheres of the close-in exoplanets however can be significantly different compared to those of the Galilean satellites. The interaction with these atmospheres and the planetary magnetic field is expected to generate plasma and magnetic field perturbations qualitatively similar to the moons of Jupiter. If the exoplanets possess electrically conductive layers, any time-variable external

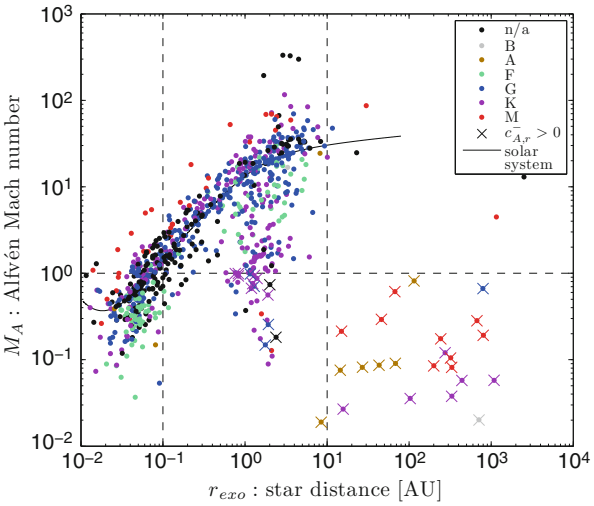

Fig. 6.1 Estimated Alfvén Mach numbers M_A near all 850 extrasolar planets known until 2013. For all extrasolar planets with $M_A < 1$ no bow shock forms, which is the case for most of the planets located within 0.1 AU of their host star (from Saur et al. 2013)

magnetic field will additionally induce secondary magnetic fields similar to the mechanisms at the Galilean satellites. Extrasolar planets at stellar separation larger than approximately 0.1 AU are on average subject to super-Alfvénic conditions ($M_A > 1$) and thus are expected to possess bow shocks if additionally $M_f > 1$ similar to Jupiter. Thus the interactions in the Jupiter system are textbook cases for the interactions at extrasolar planets with the benefit that a huge set of in-situ and remote-sensing observations are available. Thus an improvement of our understanding of the plasma and magnetic field environments in the Jupiter system is helpful as this understanding is also relevant for extrasolar planets.

6.2.1.2 The Planetary Body: Nature of the Obstacle

The nature of the planetary body, i.e., the obstacle to the flow, shapes the plasma and magnetic field environment in particular very close to the planetary body. The body can be a mechanical obstacle, e.g., due to collisions of the neutral particles in the atmosphere with the plasma or if the body possesses a solid surface. The body can also be an electromagnetic obstacle, e.g., if it possesses an internal magnetic field or if it is electrically conductive. The Galilean satellites are a mix of both mechanical and electromagnetic obstacles. They all possess very dilute atmospheres and solid, plasma absorbing surfaces. Among the Galilean satellites, Ganymede is the strongest electromagnetic obstacle because it possesses an internal dynamo magnetic field, which generates a mini-magnetosphere within Jupiter's large magnetosphere (Kivelson et al. 1996). But electrically conductive layers within all of the moons, e.g. saline oceans, metallic cores or a possible magma ocean, generate induced magnetic fields, which influence the external space and plasma environment around all of these moons (e.g., Khurana et al. 1998; Neubauer 1998; Khurana et al. 2011; Seufert et al. 2011).

6.2.2 MHD Model

The most common approach to describe the interaction of a planetary body within its surrounding plasma is the MHD approach. It describes the plasma as an electrically conductive fluid and is applicable to describe the overall properties of the interaction if typical length scales of the interaction are larger than the ion gyro radius and typical time scales are larger than the ion gyro period.

The MHD approach applies to describe the temporal and spatial evolution of the mass density ρ_m the continuity equation, for the plasma bulk velocity $\mathbf{v}$ the velocity equation, for the magnetic field $\mathbf{B}$ the induction equation, and an equation for the

internal energy ϵ, respectively,

$$\partial_t \rho_m + \nabla \cdot (\rho_m \mathbf{v}) = (P - L) m_i \ , \tag{6.1}$$

$$\rho_m \partial_t \mathbf{v} + \rho_m \mathbf{v} \cdot \nabla \mathbf{v} = -\nabla p + \left(\frac{1}{\mu_0} \nabla \times \mathbf{B} \right) \times \mathbf{B} - (\rho_m \nu_{in} + P m_i) \mathbf{v} \ , \tag{6.2}$$

$$\partial_t \mathbf{B} = \nabla \times (\mathbf{v} \times \mathbf{B}) + \eta \Delta \mathbf{B} \ , \tag{6.3}$$

$$\partial_t \epsilon + \nabla \cdot (\epsilon \mathbf{v}) = -p \nabla \cdot \mathbf{v} + \frac{1}{2} \rho_m \mathbf{v}^2 \left(\frac{P}{n} + \nu_{in} \right) - \epsilon \left(\frac{L}{n} + \nu_{in} \right) \ . \tag{6.4}$$

The continuity equation (6.1) can include sources P due to ionization of neutral particles with mass m_i and losses L due to recombination. The velocity equation (6.2) includes in case of a mechanical obstacle the collisions and the mass loading in an atmosphere of the planetary body with ν_{in} the collision frequency for momentum transfer between the ions and the neutrals through elastic collisions and charge exchange. Here we assumed that the velocity of the atmosphere is at rest. The evolution of the magnetic field is described by the induction equation (6.3), which can include a resistive term characterized by the magnetic diffusivity η. The evolution of the internal energy density ϵ, which is related to the plasma thermal pressure p through $\epsilon = 3/2\, p$ is described through (6.4). The total thermal pressure p includes the effects of the electron temperature T_e and the ion temperature T_i by $p = n k_B (T_e + T_i)$ with the Boltzmann constant k_B, and the plasma number density n. The MHD approach does however not allow to constrain the T_e and T_i separately without further assumptions. In (6.4), next to the work done by the pressure, the collisions of the plasma with neutrals as well as plasma production and recombination are included.

In order to describe the interaction as a well-posed problem, initial and boundary conditions need to be specified. For the initial conditions, the unperturbed plasma or approximations to the final solutions are generally used. The outer boundary conditions are chosen so that on the upstream side of the obstacle inflowing conditions are set. They characterize the properties of the plasma flow upstream of the obstacle. Downstream of the obstacle outflowing boundary conditions are applied (e.g., Chané et al. 2013; Duling et al. 2014). The inner boundary for the plasma is located at the surface of the planetary body if the plasma reaches all the way to the surface (Duling et al. 2014). For a planet with a very dense atmosphere such as Jupiter, the inner boundary is located below the ionosphere (Chané et al. 2013). In case of the moons, the plasma is absorbed at the surfaces of the solid bodies, which are additionally assumed to be no source of plasma. These conditions imply that the radial component of the plasma flow v_r can only be negative or zero, which also sets the conditions for the plasma, momentum, and energy flow in Eqs. (6.1), (6.2), and (6.4) (Duling et al. 2014). In case of Jupiter the inner boundary conditions for the plasma is such that $v_r = 0$ (Chané et al. 2013). The boundary condition for the magnetic field is given by the electrically non-conductive nature of the solid surface of the moons and the neutral atmosphere below Jupiter's

ionosphere. This insulating nature implies that the radial component of the electric current at the boundary needs to vanish, i.e., $j_r = 0$. The latter condition has non-local effects on the magnetic field and can be implemented by decomposing the magnetic field at the surface into poloidal and toroidal fields, which are expended into spherical harmonics. Duling et al. (2014) showed that for the resulting complex poloidal and toroidal coefficients p^*_{lm} and t^*_{lm} of the spherical harmonics Y^*_{lm} of degree l and order m, respectively, the following two equations need to be fulfilled

$$t^*_{lm}(R_0, t) = 0, \tag{6.5}$$

$$R_0 \frac{\partial p^*_{lm}(r,t)}{\partial r}\bigg|_{r=R_0} - (l+1)p^*_{lm}(R_0,t) = -\frac{2l+1}{l} G^*_{lm}(t). \tag{6.6}$$

These equations need to be fulfilled at the inner boundary at every time step and thus set the magnetic field boundary conditions at the surface located at R_0. This description of the inner boundary conditions for the magnetic field also allows that the planetary body possesses internal magnetic fields whose origin lie below the surface. They can be internal dynamo fields as is the case for Jupiter and Ganymede, but they can also be time-variable induction magnetic fields generated in saline electrically conductive subsurface oceans. The internal fields are represented in (6.6) through their complex Gauss coefficients $G^*_{lm}(t)$. In case of Jupiter and its very strong magnetic field, the inner boundary conditions can be approximated by setting the azimuthal and the longitudinal component of the magnetic field to the internal Jovian magnetic field (Chané et al. 2013).

The MHD approach is overall a very powerful approach to describe the plasma dynamics in the Jupiter system. Naturally, it does not capture all aspects of the plasma interaction, e.g., if electron scale physics is relevant and/or gyro radii and gyro periods need to be resolved. For example, reconnection at the magnetopauses of Jupiter and Ganymede is a non-ideal MHD effect which is best described with models which resolve ion and electron kinetics, e.g., with full particle-in-cell models. Finite gyro radii effects can play a role in situations where non-thermal, high energy ions are involved or where ions with large velocities within a small background magnetic field are picked-up. In case the latter effects are important, appropriate models are hybrid models or particle-in-cell models. Even though MHD models cannot resolve ion and electron kinetics effects, one of their advantages in numerical simulations is that they generally enable better spatial resolutions compared to kinetic models in case of similar computational resources. This advantage is particularly helpful if small atmospheric scale heights need to be resolved.

6.3 Jupiter's Magnetosphere

Jupiter's magnetosphere is qualitatively different compared to the magnetosphere of the Earth. The magnetosphere of Jupiter is rotationally dominated throughout a large part of the magnetosphere and the moons of Jupiter are huge internal mass sources (e.g., Vasyliūnas 1983; Bagenal and Delamere 2011). Io provides approximately $10^3\,\mathrm{kg\,s^{-1}}$ mostly in form of SO_2 and Europa approximately $50\,\mathrm{kg\,s^{-1}}$ in form of O_2 to the magnetosphere (e.g., Broadfoot et al. 1979; Saur et al. 1998, 2003; Mauk et al. 2003). This mass is subsequently being ionized and picked up by the motional electric field of the fast rotating magnetosphere. Jupiter's sideric rotation period is $\sim$9.9 h. The plasma thus experiences large centrifugal forces responsible for radial transport of the plasma. Due to conservations of angular momentum the magnetospheric plasma while being transported radially outward is not rigidly corotating anymore. This sets up magnetic stresses and electric current systems which couple the magnetosphere to Jupiter's ionosphere. Through this coupling angular momentum is being transported from Jupiter's ionosphere into Jupiter's magnetosphere to bring the magnetosphere closer to full corotation. Jupiter's magnetosphere and its internal coupling has been described theoretically and numerically by a series of authors (e.g., Hill 1979; Vasyliūnas 1983; Hill 2001; Cowley and Bunce 2001; Southwood and Kivelson 2001; Ogino et al. 1998; Walker and Ogino 2003; Moriguchi et al. 2008; Ray et al. 2010).

Because of the immense importance of Jupiter's magnetosphere-ionosphere (MI) coupling, Chané et al. (2013) developed a new MHD model of Jupiter's magnetosphere. This model explicitly includes the ionosphere of Jupiter within the model domain. In Jupiter's ionosphere ion-neutral collisions transfer angular momentum from the neutrals onto the plasma. The resultant flow generates magnetic stresses between the ionosphere and magnetosphere, which accelerate the magnetosphere in the direction of Jupiter's rotation, but decelerate Jupiter's ionosphere in return. In the model of Chané et al. (2013) the MI-coupling is explicitly included and the magnetic field boundary conditions can be physically correctly set below the ionosphere (see Sect. 6.2.2). The downside of the approach is that for numerical reasons, the radial extension of the ionosphere is strongly exaggerated by 4 Jovian radii (R_J) and the surface of Jupiter has been set to be at 4.5 R_J. Despite the latter assumption, the Chané et al. (2013) model however still uses the closest inner boundary of all published MHD models of Jupiter's magnetosphere. The model includes the mass loading in the Io plasma torus explicitly. It thus explicitly includes two of the most important features of Jupiter's magnetosphere: The coupling to the ionosphere and the mass loading in a fast rotating magnetosphere.

The overall density and magnetic field structure of the modelled magnetosphere is shown in Fig. 6.2. The bow shock is located at 73 R_J and the magnetopause at 69 R_J in agreement with in-situ measurements (Joy et al. 2002). The magnetosphere is compressed on the day side and strongly elongated on the night side. Figure 6.2 also shows an X-point on the night side where a plasmoid of plasma is being released as part of the mass loss processes in the tail of the magnetosphere. The figure also

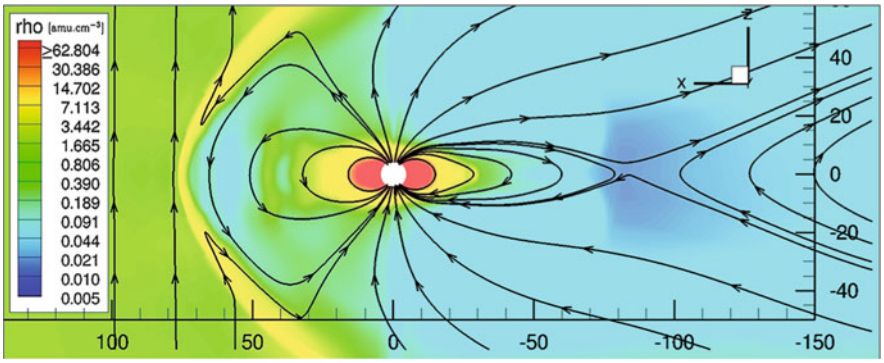

Fig. 6.2 Density contours in the noon-midnight meridian of Jupiter's magnetosphere. The solar wind is coming from the left. The magnetic field lines are shown in *black* (from Chané et al. 2013)

shows that the plasma is concentrated in the equatorial regions of the magnetosphere due to the strong centrifugal forces. The radial density profile of the Chané et al. (2013) model agrees very well with measured density profiles taken by the Galileo spacecraft (Frank et al. 2002; Bagenal and Delamere 2011).

In Fig. 6.3, the electric current system which represents the angular momentum transfer between Jupiter's ionosphere and magnetosphere is displayed. The electric current loop connects Jupiter's ionosphere through field aligned currents directed away from Jupiter and which are fed into the equatorial plasma sheet of Jupiter's magnetosphere at radial distances of 20 to 30 R_J. In this plasma sheet the currents are directed mostly radially outward and the related $\mathbf{j} \times \mathbf{B}$ forces spin up the magnetosphere. The current closure back to the ionosphere occurs at large radial distances (not clearly visible at low latitudes in Fig. 6.3) and enter the ionosphere in the polar region. The $\mathbf{j} \times \mathbf{B}$ forces slow the plasma in the ionosphere and are in balance with the forces exerted by the ion-neutral collisions, which accelerate the ionosphere.

The modeled azimuthal and radial velocities in Chané et al. (2013) are in good agreement with observations by the Galileo and Voyager spacecraft and the theoretical predictions by Hill (1979). In Fig. 6.4 the modeled azimuthal velocities as a function of radial distance are shown for various mass loading rates in comparison to Voyager measurements. The corotation breakdown (as defined by Hill (1979), 75% of rigid corotation) in the plane of Fig. 6.3 occurs at a radial distance of 32 R_J, but the plasma starts to subcorotate at approximately 20 R_J. These results are consistent with the locations of the field-aligned currents and match the theoretical predictions obtained for the same ionospheric conductances and total radial mass transport rates by Hill (1979, 2001).

On field lines with large parallel electric currents pointing away from the planet and on locations along these field lines where the charge carrier density is small, electrons need to be accelerated to large energies to maintain the electric current

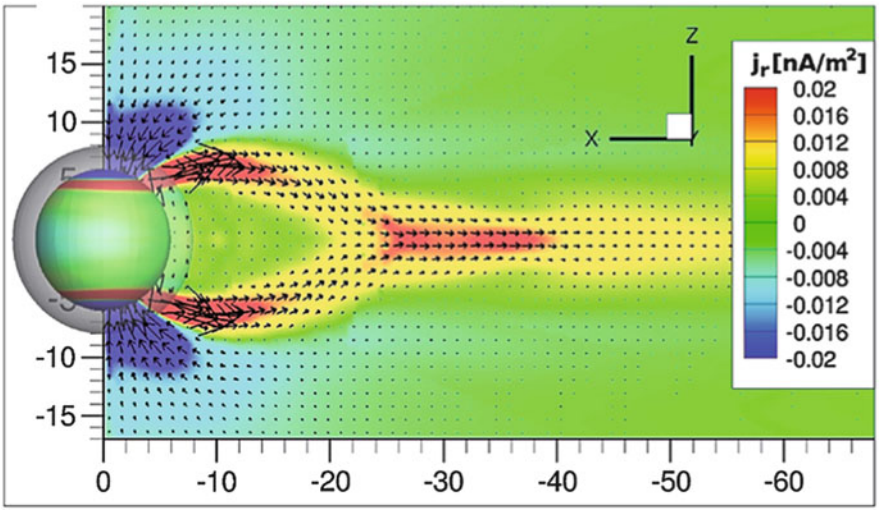

Fig. 6.3 Corotation enforcing current system on the night side of Jupiter in the noon-midnight meridian. The radial current is shown with color contours, and the direction of the current in the same plane is represented by the *black arrows*. The radial current in the ionospheric region is displayed on a sphere at 6 R_J, and a transparent sphere at 8 R_J shows the extent of the ionospheric region. Note that the corotation breakdown of rigid corotation in this plane occurs at 32 R_J (from Chané et al. 2013)

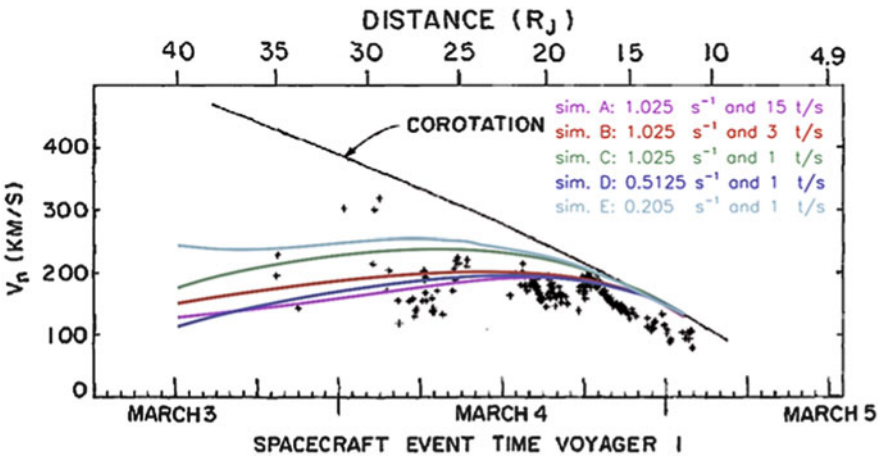

Fig. 6.4 Azimuthal velocity as a function of radial distance: Comparison between Voyager I measurements (*black plus signs*) and computational results (*color lines*). The model output values are over plotted on top of Figure 6.24 from Khurana et al. (2004), which was adapted from McNutt et al. (1981). The model values are shown for different Io torus mass loading rates and ionospheric ion-neutral collision frequencies. The *black line* represents rigid corotation. For the computations, the values given are for the equatorial plane and were averaged over a rotation period and over all local times (from Chané et al. 2013)

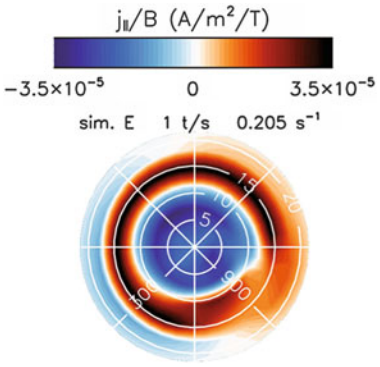

Fig. 6.5 Color contours show $j_{\parallel}/B$ in Jupiter's northern hemisphere at 1 R_J. The values of the current were projected from the ionosphere to a sphere at 1 R_J by following the dipole magnetic field lines. The value of $j_{\parallel}/B$ is averaged over a rotation period. The colatitude and the local time are plotted in *white* on the figures; the dayside is located on the right (from Chané et al. 2013)

loop (Knight 1973; Hill 2001; Cowley and Bunce 2001). The resultant energetic electrons precipitate into Jupiter's ionosphere and excite Jupiter's main auroral oval, which has been extensively observed, e.g., with the Hubble Space Telescope (HST) (e.g., Clarke et al. 2005). Therefore the location in Jupiter's atmosphere, where field lines with large anti-planetward electric current densities map to, can be associated with auroral emission. In Fig. 6.5 we show the electric current density from the Chané et al. (2013) model mapped along dipole field lines into Jupiter's atmosphere. The images show that the current system matches to colatitudes of approximately 15°, which is in good agreement with observations (e.g., Clarke et al. 2005). Figure 6.5 also shows that the electric current is azimuthally asymmetric as expected from a magnetosphere with strong local-time asymmetries. In particular, between 8:00 and 11:00 LT the anti-planetward electric current density has a minimum, which is consistent with a discontinuity in the main oval observed by Radioti et al. (2008) within HST observations. The discontinuity in the electric current in the model of Chané et al. (2013) is caused by an asymmetry in the pressure distribution due to the interaction between the rotating plasma and the magnetopause.

6.4 Time-Variable Magnetosphere

While we discussed in the previous section mostly steady state components of Jupiter's magnetosphere, we address here magnetospheric time-variability caused by the solar wind, by variations of the internal sources, by the rotation of Jupiter, and by dynamical non-linear processes in the magnetosphere.

The internal plasma sources of Jupiter's magnetosphere, i.e., the mass loading at the moons might be time-variable which is however observationally not established

very well. The model of Chané et al. (2013) shows that if the mass loading rate of Io changes from 1×10^3 to 3×10^3 kg s^{-1}, the azimuthal velocity profile changes and the breakdown of corotation occurs further inside (see Fig. 6.4). The change in the mass loading also implies changes in the size of the magnetosphere, the structure of the magnetic field, and in the field aligned auroral current systems. For enhanced mass-loading rates, Chané et al. (2013) find that the auroral becomes more symmetric, while the brightness barely changes.

Changing solar wind conditions impacts Jupiter's magnetosphere as well. An increase in solar wind ram pressure decreases the size of the magnetosphere on the subsolar direction and stretches it towards the night side. An important question is how the auroral brightness responds to an increased ram pressure. Earlier theoretical work by Cowley and Bunce (2001), Southwood and Kivelson (2001), and Cowley and Bunce (2003) suggested that the aurora dims in this case because the decreased size of the magnetosphere moves the magnetospheric plasma somewhat radially inward, leading to increased angular velocities (since the angular momentum is conserved). This is expected to reduce the corotational enforcing electric currents and thus to lead to a reduced auroral brightness. The simulations of Chané et al. (2013) predict that the overall response to increased solar wind ram pressure strongly depends on local time, but leads in general to an overall increased auroral brightness (Chané et al. 2017). The primary reason is that the enhanced solar wind ram pressure increases the magnetic stresses in the magnetosphere leading to higher field-aligned electric currents. For deriving these results, the three-dimensional nature of the magnetosphere needs to be considered. Chané et al. (2017) find that only for a short period of time, during the transition phase from weak to strong solar wind ram pressure the aurora locally dims in the noon region.

Another cause of time-variability are dynamical processes in the magnetosphere. Among these processes are intermittent reconnection on the night side and the release of plasmoids on time scales on the order of 10 h (Bagenal 2007; Chané et al. 2013; Vogt et al. 2014; Chané et al. 2017). The radial transport within the magnetosphere occurs through flux tube interchange (e.g., Kivelson et al. 1997). The resultant perturbations of the magnetosphere are stochastic in nature. These perturbations in turn interact with each other generating a turbulent cascade of time-dependent magnetic field and velocity fluctuations (Saur et al. 2002).

Another class of time-variability is induced in Jupiter's magnetosphere due to the approximately 10° tilt of Jupiter's magnetic moment with respect to its spin axis. This tilt makes all properties of Jupiter's magnetosphere time-variable with a period of the sideric rotation period of Jupiter (9.9 h) when observed in an inertial rest frame. This time-variability is important for the magnetosphere itself, but it also leads to time-variable magnetic fields at the locations of the moons, which can be used to probe their interior structure (e.g., Khurana et al. 1998; Neubauer 1998; Kivelson et al. 2000; Zimmer et al. 2000).

The time-variability of the magnetic field near the Galilean moons has been explored extensively by Seufert et al. (2011) through considerations of a range of possibly frequencies. The magnetic field model of Seufert et al. (2011) includes (a) the dynamo magnetic field of Jupiter represented by an expansion in spherical

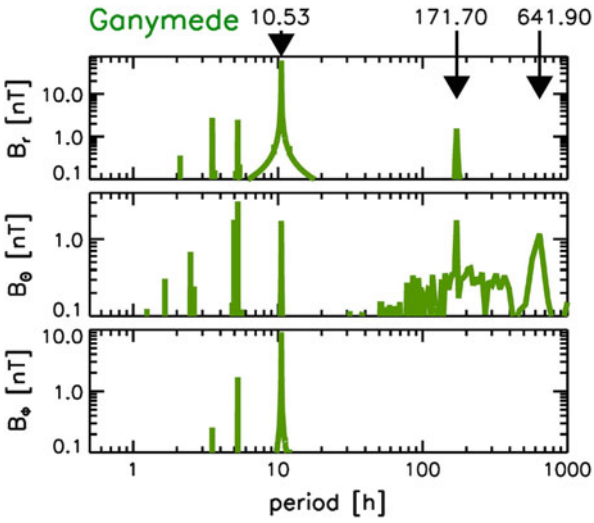

Fig. 6.6 Amplitudes of the time-variable radial B_r, azimuthal B_Φ, and latitudinal B_Θ magnetic field components of Jupiter's magnetosphere at the location of Ganymede. The period 10.53 h is the synodic rotation period of Jupiter as seen from Ganymede, 171.7 h is the orbital period of Ganymede, and 641.9 h is solar rotation period (from Seufert et al. 2011)

harmonics, (b) the magnetic fields of the current sheet, and (c) fields due to the magnetopause boundary currents. With this magnetic field model, field components at the location of the moons are calculated and subsequently Fourier-transformed to obtain the time-variable magnetic field amplitudes as a function of their period as shown in Fig. 6.6. The figure shows three sources of time-variability at Ganymede, i.e., three sets of periods: (1) the rotation period of Jupiter and higher harmonics thereof due to non-dipole components of the interior field and due to non-sinusoidal components of the current sheet field. The synodic rotation period of Jupiter seen in the restframe of the satellites generates the strongest amplitudes of all periods with the maximum in the B_r component of $\sim$80 nT (Seufert et al. 2011). The higher order harmonics are already significantly smaller on the order of a few nT or less. (2) The time-periodic contribution due to the orbital period of Ganymede is fairly small on the order of 1–2 nT due to the small inclination $i = 0.17°$ and small eccentricity $e = 0.0011$ of Ganymede. (3) The solar rotation period of the sun is propagated out through the solar wind and can generate time-variable solar wind ram pressure, which generates time-variable magnetopause currents also called Chapman-Ferraro currents. The related currents cause amplitudes in the latitudinal B_Θ components of less than 1 nT. We will see in Sect. 6.5 that these various time-dependent fields generate induced magnetic fields in the interior of Ganymede. Observations of these induced magnetic field with the knowledge of the time-variable inducing fields from Fig. 6.6 or previous studies, e.g., by Kivelson et al. (2002) can be used to probe the interior of Ganymede and the other moons. Seufert et al. (2011) calculate the amplitudes and the phases of the induced magnetic fields for the three inducing frequencies and for various models of the electrical conductivity structure within Ganymede, e.g., with a poorly conductive surface, a conductive saline subsurface water ocean and very highly conductive metallic core.

6.5 Ganymede's Magnetosphere

Ganymede is the largest moon in the solar system and comparable in size to Mercury. It is also the only known moon with an intrinsic dynamo magnetic field. Thus it possesses a mini-magnetosphere within Jupiter's gigantic magnetosphere as studied by a number of authors, e.g., Kivelson et al. (1998, 2002), Kopp and Ip (2002), Ip and Kopp (2002), Paty and Winglee (2004, 2006), and Paty et al. (2008), Jia et al. (2008, 2009, 2010).

With the new MHD model developed for Ganymede by Duling et al. (2014) and introduced in Sect. 6.2.2, we model Ganymede's plasma and magnetic field environment as displayed in Fig. 6.7. The MHD model includes Ganymede's internal dynamo magnetic field after Kivelson et al. (2002) and induction in a subsurface ocean through the non-conducting boundary conditions given in Eqs. (6.5) and

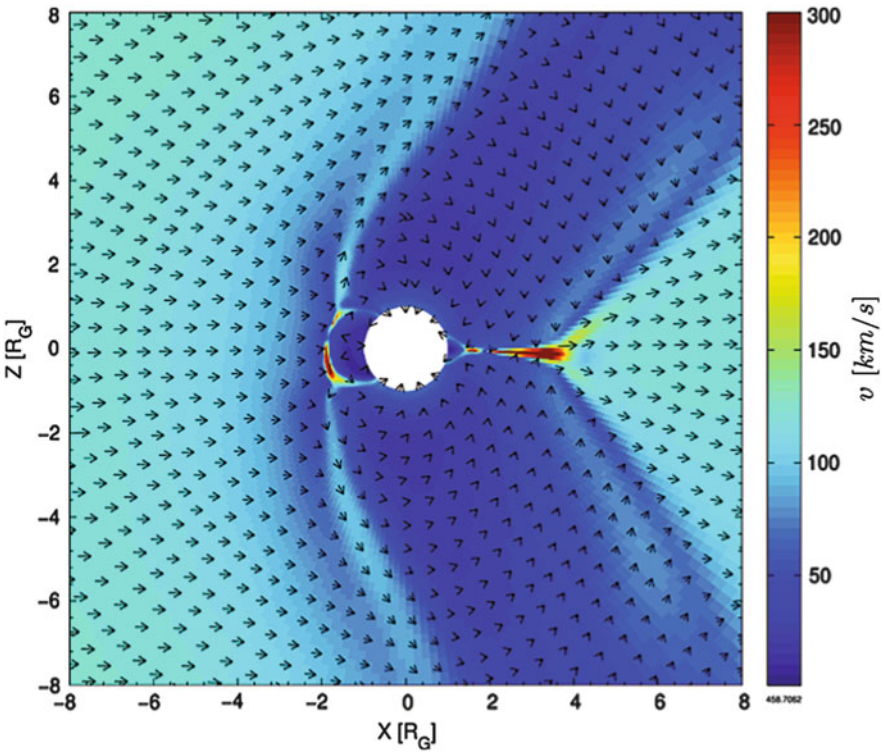

Fig. 6.7 Plasma velocity **v** around Ganymede in a plane perpendicular to the direction Ganymede-Jupiter, i.e., the plane given by the unperturbed plasma flow and the north-south direction (for the conditions of Galileo spacecraft G8 flyby). The *length of an arrow* in this figure represents the magnitude of the vector components within the displayed plane. The total magnitude of the vector is displayed color coded. In this figure the color bar is caped while maximum values of $\sim$460 km s^{-1} are reached in the *dark red* regions (from Duling et al. 2014)

(6.6). The model uses appropriate outer boundary and initial conditions given by the Galileo spacecraft measurements during each of its flybys at Ganymede. The model also includes a thin atmosphere, in which ionization with a constant ionization frequency generates an ionosphere as a source term in Eq. (6.1). Elastic collisions, charge exchange, and ionization slow the flow in the ionosphere, which is implemented in the source terms in the velocity equation (6.2). In the induction equation (6.3), we include the resistivity of the ionosphere and anomalous resistivity due to reconnection similar to Jia et al. (2010).

An appropriate description of the magnetic boundary condition at the surface of Ganymede (see Sect. 6.2.2) is crucial to correctly describe Ganymede's magnetic field environment. Commonly applied incorrect boundary conditions are to set the magnetic field at the surface of Ganymede to fixed values given by the internal magnetic field. This approach forces the plasma magnetic fields to be zero and allows electric current to enter through the electrically non-conducting surface of Ganymede. In Fig. 6.8, we show the magnetic field perturbations at the surface of Ganymede, which would be neglected if the magnetic field at surface is set to the values of the dynamo field. The plasma magnetic field assumes values up to ∼120 nT. These values are larger than the time-variable components and the induction effects of an ocean and are about 20% of Ganymede's dynamo magnetic field. Thus applying incorrect boundary conditions significantly distorts the magnetic field environment around Ganymede.

The relative velocity of Jupiter's magnetospheric plasma with respect to Ganymede is sub-Alfvénic (e.g., Neubauer 1998) and thus no bow shock forms. Ganymede's internal magnetic field generates a mini-magnetosphere with a region of closed magnetic field lines as can be seen as the green shaded region in the top

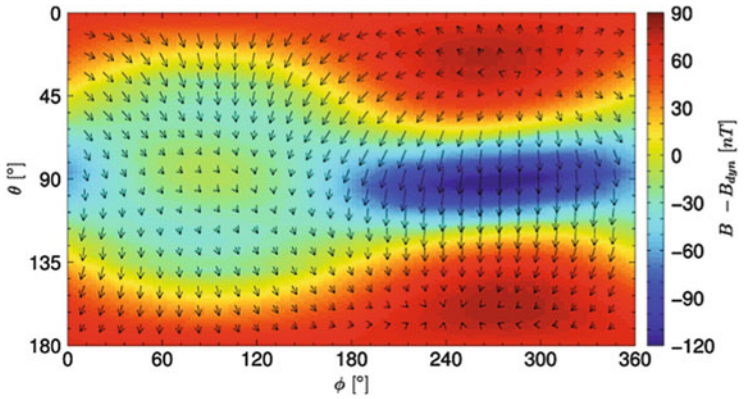

Fig. 6.8 Magnetic field components caused by the plasma interactions at Ganymede's surface. Color coded is the difference of the magnitude of the simulated total magnetic field and the magnitude of Ganymede's dynamo-generated magnetic field that is given by the dipole Gauss coefficients in Kivelson et al. (2002). The *arrows* show the tangential components of the plasma magnetic field (from Duling et al. 2014)

panel of Fig. 6.9. The closed field line region is shifted towards higher latitudes on the upstream side and is shifted towards the equator on the downstream side due to the magnetic stresses acting on Ganymede (Neubauer 1998). This effect is also well visible in Fig. 6.7. The same figure additionally shows that the plasma flow within the closed field line region is reversed, i.e., in the upstream direction compared to the unperturbed magnetospheric flow.

Due to the sub-Alfvénic nature of the incoming flow Alfvén wings form, which are displayed as blue region in the top panel of Fig. 6.9. The Alfvén wings are also visible in Fig. 6.7 as the large structures north and south of Ganymede where the plasma flow is strongly reduced. The width of the Alfvén wings is significantly larger compared to Ganymede and the width of the closed field region. This is due to the orientation of the internal magnetic field and the external field of Jupiter's magnetosphere. The width of the wings at the presence of an internal magnetic field shown in Fig. 6.9 is in agreement with quantitative expressions for the width derived in Neubauer (1998) and Saur et al. (2013).

In the bottom panel of Fig. 6.9 we quantitatively compare the MHD model results of Duling et al. (2014) shown in green with magnetic field measurements by the Galileo spacecraft taken during the G 29 flyby shown in red. This flyby crossed the northern Alfvén wings and is displayed as a yellow arrow in the top panel of Fig. 6.9. The MHD model fits the amplitude and locations of the wing crossing well. It also quantitatively reproduces the magnetic field measurements of all the other Ganymede flyby by the Galileo spacecraft (e.g., Duling et al. 2014).

6.6 Ganymede's Ocean

The time-periodic magnetic fields in Jupiter's magnetosphere as discussed in Sect. 6.4 can be used to explore electrically conductive layers within the moons of Jupiter (e.g., Khurana et al. 1998; Neubauer 1998; Zimmer et al. 2000). These fields establish one of the few currently available methods to search for saline and thus electrically conductive subsurface oceans. The method is based on the fact that water in its solid form possesses an electrically conductivity at least 4 orders of magnitude smaller compared to liquid water with salinities discussed in the context of the Galilean satellites (e.g., Seufert et al. 2011). The magnetic field measurements by the Galileo spacecraft near Ganymede have been searched for signs of induction signals from an ocean by Kivelson et al. (2002). It was found that the magnetic field measurements from multiple flybys are consistent with an ocean, however the measurements can be fitted quantitatively equally well by unknown quadrupole moments of Ganymede's dynamo magnetic field (Kivelson et al. 2002). Unfortunately, it is impossible to overcome this uncertainty, i.e., to separate spatial and temporal variability with subsequent flybys along different trajectories.

As discussed in Sect. 6.4 and visible in Fig. 6.6, the time-variable magnetic field component of Jupiter's magnetosphere with the largest amplitude is the B_r

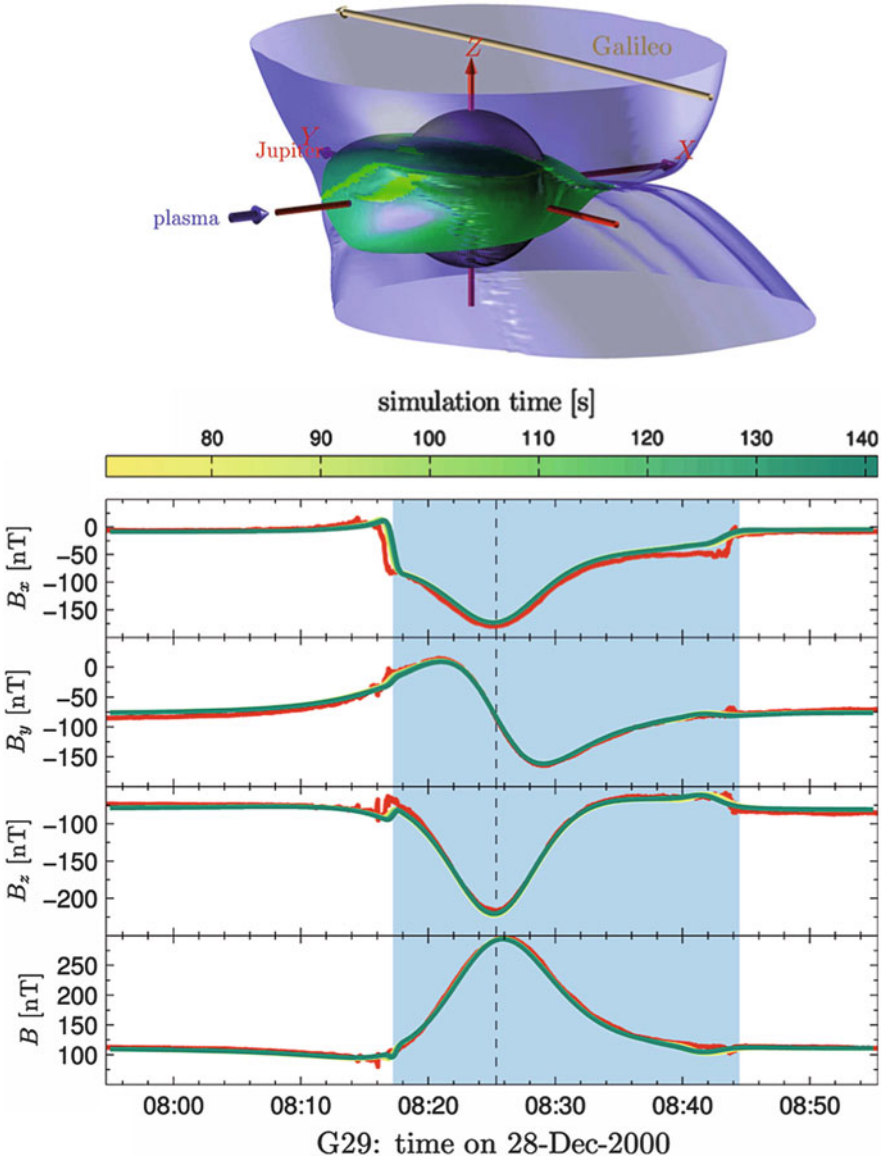

Fig. 6.9 Modeled structure of Ganymede's magnetosphere in *top panel* with closed field line region in *green* and open field line region in *blue*. Magnetic field measurements in *red* and model results in *yellow-green lines* are shown in *bottom*. Both panels are for the G 29 flyby (from Duling et al. 2014)

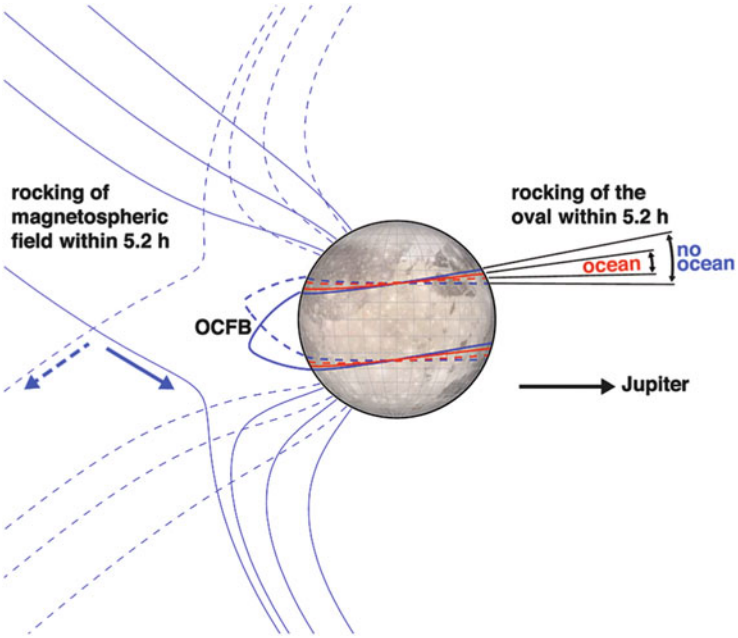

Fig. 6.10 Sketch of magnetic field lines and locations of auroral ovals when Ganymede is above (*dashed lines*) and below the current sheet (*solid lines*), respectively. The ovals are located where the open-closed field line boundary (OCFB) intersects Ganymede's surface. Induction in an ocean partly compensates Jupiter's time-variable field and thus reduces the oscillation of the ovals (*red*: with ocean; *blue*: without ocean) (from Saur et al. 2015)

component with values of ∼80 nT. In Fig. 6.10 we show a sketch of the magnetic field environment around Ganymede for maximum positive B_r, i.e., pointing away from Jupiter (dashed lines) and for maximum negative B_r, i.e., pointing towards Jupiter (solid blue lines). The time-variable exterior component also modifies the open-closed field line boundary (OCFL) region of Ganymede's magnetosphere as displayed in Fig. 6.10) as well.

Ganymede also possesses two auroral ovals (Hall et al. 1998; Feldman et al. 2000; McGrath et al. 2013) similar to all known planetary bodies with an intrinsic dynamo magnetic field and an atmosphere. An example of two auroral images taken with the Hubble Space Telescope (HST) is shown in Fig. 6.11. The two auroral ovals are located near the region where the open-closed field line region intersects with Ganymede's atmosphere as shown as red and blue lines on the surface of Ganymede in Fig. 6.10. Because the time-variable external magnetic field modifies the open-closed field line boundary, the location of the auroral ovals are time-variable as well and oscillate in the way depicted by the solid and dashed blue lines on the disk of Ganymede shown in Fig. 6.10. The dashed/solid lines represent the location of the auroral ovals when Ganymede is above/below the plasma sheet of Jupiter's magnetosphere, respectively. When a saline and thus electrically conductive ocean

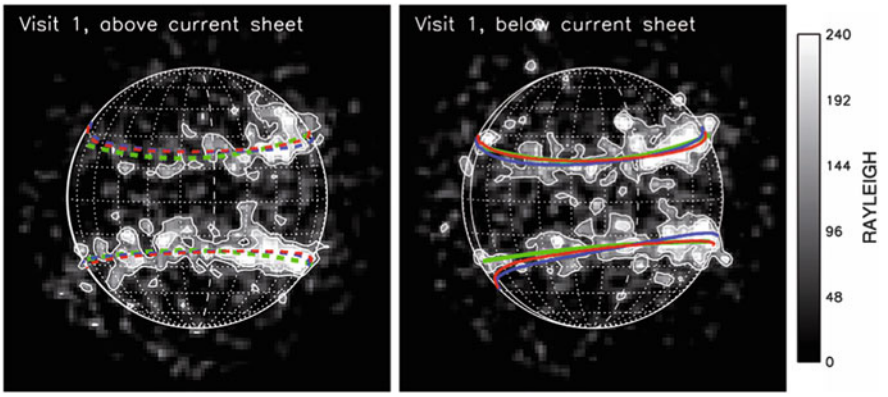

Fig. 6.11 Observed auroral brightness in Rayleigh of OI 1356 Å emission when Ganymede is (*left*) above and (*right*) below the current sheet. Contours are for 110 and 170 Rayleigh. North is up and Jupiter to the right. *Green lines* display fits to the observation, *red and blue lines* display model locations with and without ocean, respectively (from Saur et al. 2015)

is present, the time-variable external field will induce secondary magnetic fields which will reduce the primary time-variable external magnetic field. The existence of an ocean will thus also reduce the amplitude of the oscillation of the locations of the auroral ovals. The reduced oscillation amplitudes are shown in Fig. 6.10, where the solid and dashed red lines indicate the locations of the auroral ovals when an ocean is present in contrast to the blue lines when no ocean is present.

With dedicated HST observations obtained in November 2010 and October 2011, Saur et al. (2015) measured the locations of the ovals when Ganymede is maximum above and maximum below the current sheet in the search for a subsurface ocean. Figure 6.11 shows the HST observations from November 2010. Figure 6.11 also displays averaged locations of the ovals in green obtained from a polynomial fit to the observed ovals. The blue and the red lines in this figure show the expected locations of the ovals when an ocean and no ocean are present. The expected locations are calculated with the new MHD model of Ganymede by Duling et al. (2014) described in Sect. 6.5. Only from visual inspections of Fig. 6.11, it is nearly impossible to distinguish if the MHD runs with or without ocean fit better to the observations. We note that for this purpose the absolute locations of the ovals are not the important quantities, but the changes of the locations, i.e., the oscillation amplitudes (see Fig. 6.10) between the locations when Ganymede is above and below the current sheet. Therefore Saur et al. (2015) calculated these differences and associated them to an average oscillation angle, also called rocking angle α. The average rocking angle of the northern and southern ovals from the HST observations in 2010 and 2011 combined was found to be $\alpha = 2.0°$.

The observed locations of Ganymede's auroral ovals in the HST data are unfortunately patchy (see, e.g., Fig. 6.11). This patchiness is due to intermittent reconnection near Ganymede's magnetopause and due to the finite signal to noise

ratio of the counts on the individual detector pixels (Saur et al. 2015). In order to assess the error when comparing model oscillation amplitudes α with and without ocean to the observations, Saur et al. (2015) introduced a Monte-Carlo test. In the Monte-Carlo test synthetic observations with and without ocean are generated based on the MHD model of Duling et al. (2014). Therefore patchiness produced with a random generator based on the physics of the intermittent reconnection and based on the finite signal to noise of the observations were added to the modeled locations of the ovals. The resultant synthetic images appear visually very similar to the actually observed ovals (see Figure 7 in Saur et al. (2015)). Subsequently 1024 synthetic HST campaigns were generated with individually different patchy ovals. These synthetic images were then analyzed in an identical ways compared to the real data. In Fig. 6.12, the resultant distribution of the rocking angles is shown with and without ocean (red and blue distribution, respectively). It can be seen that both distribution functions barely overlap, which implies that the ocean and the non-ocean hypotheses can be well separated with this approach. The expectation value is $2.2° \pm 1.3°$ for the ocean model and $5.8° \pm 1.3°$ for the model without ocean. The uncertainties are calculated based on the one-sigma area around the expectations values in Fig. 6.12. The observed rocking angle $\alpha = 2.0°$ is thus consistent with the

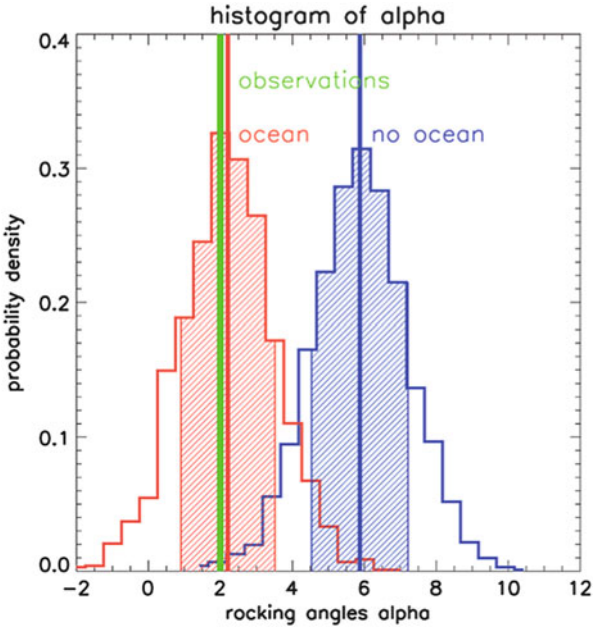

Fig. 6.12 Distribution function of modeled rocking angles α from a Monte-Carlo test with and without ocean, respectively. The test includes the effects of stochastic patchiness on the measurements. The *vertical green line* indicates rocking angle derived from observations. The *vertical red and blue lines* indicate expectation values of α, and the *shaded area* displays the 1 sigma area around the expectation values (from Saur et al. 2015)

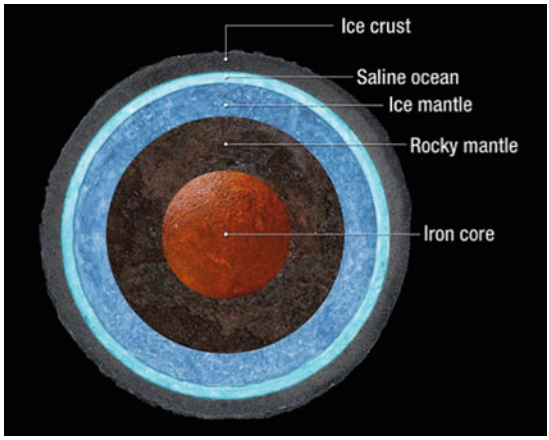

Fig. 6.13 Sketch of the internal structure of Ganymede (Image credit NASA/STScI)

existence of a subsurface ocean and inconsistent with no ocean present below the surface of Ganymede.

With this new approach the non-uniqueness of the interpretation of the Galileo magnetometer measurements by Kivelson et al. (2002) could be overcome. The key advantage of the new HST technique by Saur et al. (2015) is to search for an ocean with time-resolved two-dimensional observations of the auroral ovals, i.e. to apply time-dependent "quasi two-dimensional images" of Ganymede's magnetic field environment.

The resultant internal structure of Ganymede is shown in Fig. 6.13. The layer of liquid water is embedded within two layers of water in the solid phase. This structure is consistent with theoretical models by Sohl et al. (2002), Hussmann et al. (2006), Rambaux et al. (2011) and Vance et al. (2014). Based on the calculations in Saur et al. (2015), the ocean needs to have a minimum electrical conductivity of 0.09 S/m when assuming it to be located between 150 and 250 km depth. This conductivity corresponds to a minimum salt concentration of 0.9 g of $MgSO_4$ per kilogram ocean water. The measurement also requires that the top of the ocean cannot be deeper than 330 km when measured from the surface.

6.7 Callisto

Callisto is in size and average mass density similar to Ganymede, but structurally only a partially differentiated body (e.g., Showman and Malhotra 1999). Callisto also does not possess an intrinsic dynamo magnetic field in contrast to Ganymede. However, it encompasses similar to the other Galilean satellites a thin atmosphere and an ionosphere (Carlson 1999; Kliore et al. 2002; Cunningham et al. 2015). The time-variable components of Jupiter's magnetospheric field induce electric currents within electrically conductive layers, such as a subsurface ocean, creating

an induced dipole magnetic field based on studies by Neubauer (1998) and Zimmer et al. (2000). Callisto's atmosphere and ionosphere interact with the plasma of Jupiter's magnetosphere, which generates additional magnetic field perturbations. In the following two subsections the formation of Callisto's ionosphere and the plasma interaction will be discussed.

6.7.1 Callisto's Ionosphere

The first component of Callisto's atmosphere to be observed was CO_2 with a column density of $0.8 \times 10^{19}\,m^{-2}$ (Carlson 1999). The large ionospheric densities up to $4 \times 10^{10}\,m^{-3}$ inferred by Kliore et al. (2002) imply that an additional atmospheric component is present, which was suggested to be O_2. Hubble Space Telescope observations with the STIS camera however only led to upper limits for O_2 (Strobel et al. 2002). But subsequent observations presented by Cunningham et al. (2015) with the more sensitive HST/COS camera revealed OI 135.6 and 130.4 nm emission with a brightness of 1–5 Rayleigh. The authors derived from these observations an O_2 column density of $4 \times 10^{19}\,m^{-2}$.

A main difference of the ionosphere and the atmospheric UV emission of Callisto compared to those of the other Galilean satellites is that the plasma density of Jupiter's magnetosphere at Callisto is so dilute that electron impact is not the primary source of ionization and UV excitation anymore. Callisto's ionosphere and UV emission is in contrast primarily driven by solar photons (Cunningham et al. 2015). In order to better understand Callisto's atmosphere and ionosphere, Hartkorn et al. (2017) developed a new model to simultaneously explain the observed ionospheric electron column densities and the atmospheric UV emissions. This model solves for the electron distribution functions at every location in Callisto's atmosphere for a prescribed atmosphere which includes O_2, CO_2, and H_2O. It takes into account as the primary source of electrons the solar UV fluxes which are highly time-variable as displayed in Fig. 6.14. The model solves the Boltzmann equation for the supra-thermal electron population and considers a large set of inelastic collisions between the atmospheric species, which modifies the electron energies. As a loss for electrons recombination is included, which is energy dependent and more effective for lower electron energies. The model neglects spatial transport of the electrons, which is a good assumption for altitudes smaller than 180 km for the thermal electrons and smaller than 45 km for supra-thermal electrons (Hartkorn et al. 2017). For the low temperature electrons, i.e., energies approximately less than 0.5 eV, the electron distribution function is Maxwellian due to the importance of electron–electron collisions at these energy ranges. Therefore the model of Hartkorn et al. (2017) describes the electrons in this energy range, referred to as thermal electron range, with a fluid description for the electron particle densities and energy densities.

A resultant electron distribution function from the model of Hartkorn et al. (2017) is shown in Fig. 6.15. It demonstrates the highly non-Maxwellian nature of the

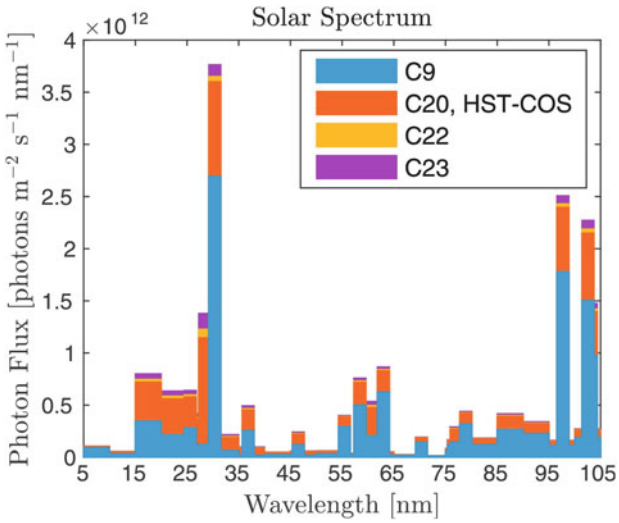

Fig. 6.14 Variability of the solar photon fluxes at Callisto's solar distance for the times of the Callisto C-9, C-20, C-22, C- 23 flybys and the HST/COS observation. The fluxes are plotted overlapping. The largest fluxes occurred during C-23 while the smallest fluxes occurred during C-9. The according dates are: C-9: 1997/06/25, C-20: 1999/05/05, C-22: 1999/08/14, C-23: 1999/09/16, HST/COS: 2011/11/17 (from Hartkorn et al. 2017)

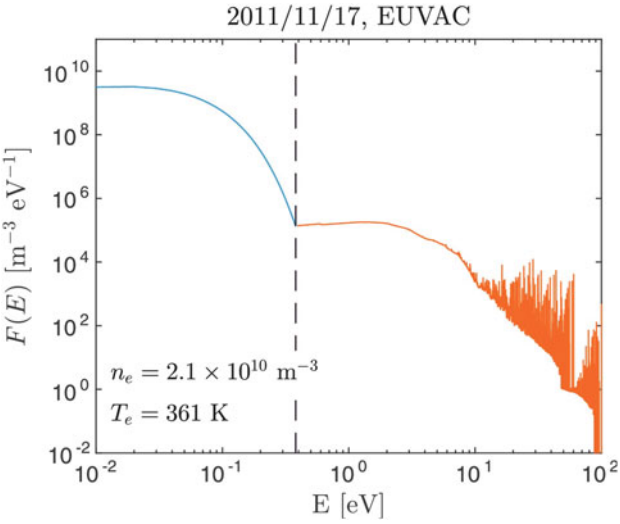

Fig. 6.15 Calculated electron energy distribution function of a volume element in Callisto's ionosphere. The prescribed neutral densities are $1.0 \times 10^{15}\,\mathrm{m}^{-3}$ for O_2 and $0.33 \times 10^{15}\,\mathrm{m}^{-3}$ for CO_2. Resulting electron density and temperature are $2.1 \times 10^{10}\,\mathrm{m}^{-3}$ and $T_e = 361$ K. The *dashed black line* marks the transition from the kinetic to the fluid range, which is located for this volume element at 0.38 eV (from Hartkorn et al. 2017)

distribution function for energies larger than 0.5 eV. This distribution function at these energies can only be calculated with a kinetic model. It shows the imprints of the solar input spectrum and the large class of possible collisional processes with the atmospheric neutrals. At lower temperature the distribution function turns Maxwellian due to the electron–electron collisions.

For a joint interpretation of the observed UV emission and the ionospheric electron densities a kinetic description of the electrons is necessary. The high energy tail of this distribution function excites the UV emission emitted from Callisto's atmosphere. With a plain Maxwellian distribution with the temperature of the thermal population barely any UV radiation would be emitted.

With the combined kinetic and fluid model, Hartkorn et al. (2017) calculate electron densities in Callisto's ionosphere. Several examples of the resultant electron density structure are displayed in Fig. 6.16. The figure also shows line of sight paths of the Galileo spacecraft radio science signals through which ionospheric electron densities were derived by Kliore et al. (2002). The radio science observations were

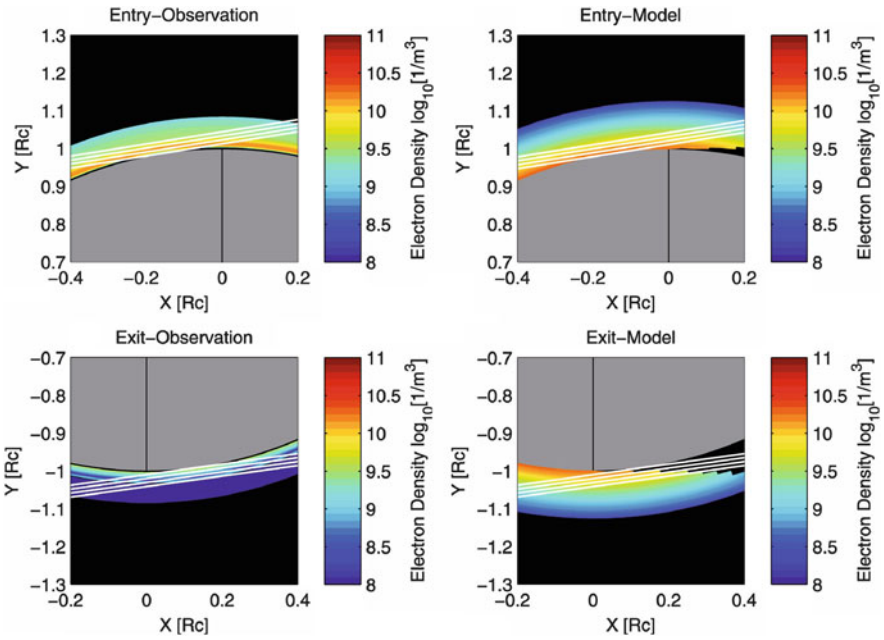

Fig. 6.16 Electron densities of the terminator regions in the equatorial plane according to the C-22 entry and exit electron density altitude profiles of Kliore et al. (2002) (*left panels*) and according to an exemplary model ionosphere with configurations of C-22 (*right panels*). For the shown model results (*right panels*), the prescribed atmosphere is spherically symmetric with an O_2 column density of $3.0 \times 10^{19}\,\mathrm{m}^{-2}$. *White lines* correspond to radio occultation LOS during entry (*upper row*) and exit (*lower row*) of flyby C-22. In this Cartesian coordinate system, the Sun is in the $-x$ direction and the y-axis is in the equatorial plane. Length scales are given in units of Callisto's radius $R_C = 2410\,\mathrm{km}$ (from Hartkorn et al. 2017)

all taken around the terminator region and thus provide constraints on Callisto's ionosphere only in this region. Because the radio science technique constrains the integral electron density along a line of sight only, this effect has to be considered when comparing model results with observations.

With the kinetic-fluid model of Hartkorn et al. (2017) the HST observations of Cunningham et al. (2015) and the electron density measurement of Kliore et al. (2002) can be jointly explained within a certain range of O_2 densities in Callisto's atmosphere. Based on this comparison, Callisto's atmosphere has a mean O_2 column density of $2.1 \pm 1.1 \times 10^{19}\,\mathrm{m}^{-2}$ and the atmosphere possesses a day night asymmetry. The terminator O_2 column density has values of $\sim 0.4 \times 10^{19}\,\mathrm{m}^{-2}$ and associated subsolar O_2 column densities are in the range of $2.4\text{–}9.8 \times 10^{19}\,\mathrm{m}^{-2}$. The calculations by Hartkorn et al. (2017) also show that the electron density is very sensitive to the relative abundance of H_2O in Callisto's atmosphere due to the thermal electron cooling by rotational state excitation of H_2O. For the efficiency of Callisto's atmospheric UV emission it is found that on average one photon is emitted at OI 135.6 nm per every 170 electron ion pairs generated and per every 60 electron ion pairs produced by secondary electron impact ionization.

6.7.2 Callisto's Plasma Interaction

Callisto with its atmosphere and ionosphere is an obstacle to the dilute plasma of Jupiter's magnetosphere streaming past the moon. This interaction is characterized by a magnetospheric space plasma environment which is more variable compared to the other Galilean satellites. The magnetospheric field $B_0 = 4\text{–}42$ nT, the relative velocity $v_0 = 122\text{–}272$ km/s, the ion density $n_0 = 0.01\text{–}0.5 \times 10^6\,\mathrm{m}^{-3}$, the Alfvén Mach numbers $\mathrm{M}_A = 0.02\text{–}1.85$, and the ion gyro radius $r_g = 34\text{–}530$ km are highly variable due to the varying position of Callisto with respect to Jupiter's magnetospheric plasma sheet and due to stochastic effects within the magnetosphere (Kivelson et al. 2004; Seufert 2012).

Seufert (2012) constructed an MHD model of Callisto's interaction with Jupiter's magnetosphere similar to the model for Ganymede described in Sect. 6.5. The model includes the formation of an ionosphere through photoionization and electron impact ionization within a pure CO_2 atmosphere and alternatively within an atmosphere composed of CO_2 and O_2. The model also includes as internal magnetic fields the induced fields from a subsurface ocean within Callisto (see Sect. 6.4). The resultant magnetic fields from the MHD model of Seufert (2012) in comparison with measurements made by the Galileo spacecraft during the C21 flyby are displayed in Fig. 6.17. The C-21 flyby was a flyby through the wake of Callisto with a closest approach of about 1000 km. In Fig. 6.17, the observed fields are shown in black and the induced magnetic field combined with the background field are shown in red. The magnetic field including the plasma interaction with a CO_2 atmosphere only is shown as green dashed line and the field from the plasma interaction with a combination of CO_2 and O_2 is shown as solid green line. The

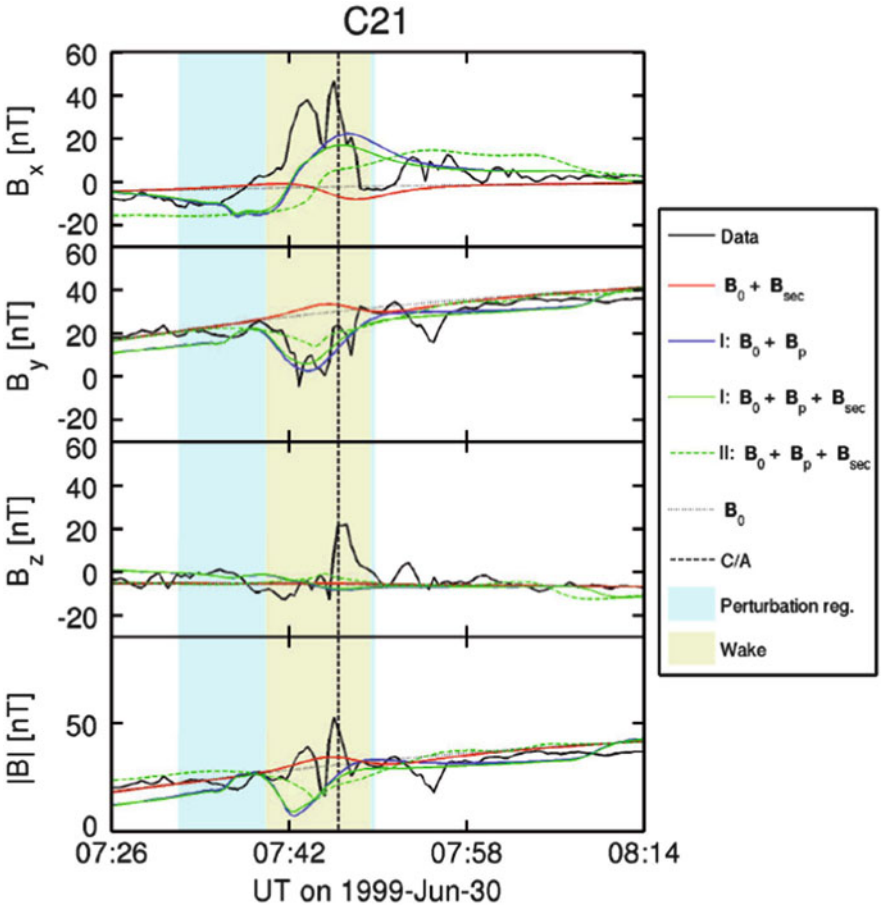

Fig. 6.17 Magnetic field measurements along the C-21 fly trajectory of the Galileo spacecraft (*black solid lines*) in comparison with modeled magnetic fields in nT. The superposition of the background magnetic field (*black dotted lines*) and the induced fields is shown in *red*. The *blue solid lines* depict a superposition of the background field and the modeled plasma interaction fields for a model (case I) using the measured plasma data with a velocity artificially decreased by a factor of five. The *green solid lines* represent a superposition of the plasma interaction and the induced fields for the case I as well. The *green dashed lines* give a similar superposition for the default model in Seufert (2012), i.e., using a corotational plasma velocity of 192 km/s (case II). *Blue and ocher* areas indicate the locations where the perturbation region and the geometrical wake for case I are crossed by the spacecraft trajectory. The *vertical dashed line* indicates the time of the closest approach (from Seufert 2012)

results demonstrate that both induction in a conductive ocean and the plasma interaction produce significant magnetic field perturbations. Similar conclusions have been reached by subsequent modeling of Liuzzo et al. (2015, 2016). Therefore an appropriate modeling of the plasma interaction and the induction effects is

necessary in the interpretation of the plasma and field measurements obtained by the Galileo spacecraft.

6.8 Summary

In this chapter, we discussed similarities and differences between the largest and one of the smallest magnetosphere in the solar systems, i.e., those of Jupiter and Ganymede. We introduced two new models for the description of their magnetic field and plasma environments. These models cover two classes of the plasma interaction between a magnetized body with its surrounding space plasma, i.e., sub-Alfénic and super-fast interactions, which have counterparts at extrasolar planets. We also showed how HST observations in conjunction with MHD modeling of Ganymede's auroral ovals can be used to search for a subsurface ocean within Ganymede. We additionally investigated the non-Maxwellian nature of the electron distribution function in Callisto's ionosphere to constrain its atmosphere based on HST and Galileo spacecraft measurements.

References

Bagenal, F.: The magnetosphere of Jupiter: coupling the equator to the poles. J. Atmos. Sol. Terr. Phys. **69**, 387–402 (2007). doi:10.1016/j.jastp.2006.08.012

Bagenal, F., Delamere, P.A.: Flow of mass and energy in the magnetospheres of Jupiter and Saturn. J. Geophys. Res. Space Phys. **116**, A05209 (2011). doi:10.1029/2010JA016294

Baumjohann, W., Treumann, R.A.: Basic Space Plasma Physics. Imperial College Press, London (1996)

Broadfoot, A.L., et al.: Extreme ultraviolet observations from Voyager 1 encounter with Jupiter. Science **204**, 979–982 (1979)

Carlson, R.: A tenuous carbon dioxide atmosphere on Jupiter's moon Callisto. Science **283**, 820–821 (1999)

Chané, E., Saur, J., Neubauer, F.M., Raeder, J., Poedts, S.: Observational evidence of Alfvén wings at the Earth. J. Geophys. Res. Space Phys. **117**(A16), A09217 (2012). doi:10.1029/2012JA017628

Chané, E., Saur, J., Poedts, S.: Modeling Jupiter's magnetosphere: influence of the internal sources. J. Geophys. Res. Space Phys. **118**, 2157–2172 (2013). doi:10.1002/jgra.50258

Chané, E., Raeder, J., Saur, J., Neubauer, F.M., Maynard, K.M., Poedts, S.: Simulations of the Earth's magnetosphere embedded in sub-Alfvénic solar wind on 24 and 25 May 2002. J. Geophys. Res. Space Phys. **120**, 8517–8528 (2015). doi:10.1002/2015JA021515

Chané, E., Saur, J., Poedts, S., Keppens, R.: How is the Jovian main auroral emission affected by the solar wind? J. Geophys. Res. Space Phys. **122**, 1960–1978 (2017). doi:10.1002/2016JA023318

Christensen, U.R., Holzwarth, V., Reiners, A.: Energy flux determines magnetic field strength of planets and stars. Nature **457**, 167–169 (2009). doi:10.1038/nature07626

Clarke, J.T., Gérard, J.C., Grodent, D., Wannawichian, S., Gustin, J., Connerney, J., Crary, F., Dougherty, M., Kurth, W., Cowley, S., Bunce, E., Hill, T., Kim, J.: Morphological differences between Saturn's ultraviolet aurorae and those of Earth and Jupiter. Nature **433**, 717–719 (2005)

Cowley, S.W.H., Bunce, E.J.: Origin of the main auroral oval in Jupiter's coupled magnetosphere-ionosphere system. Planet. Space Sci. **49**, 1067–1088 (2001)
Cowley, S.W.H., Bunce, E.J.: Modulation of Jupiter's main auroral oval emissions by solar wind induced expansions and compressions of the magnetosphere. Plant. Space Sci. **51**, 57–79 (2003). doi:10.1016/S0032-0633(02)00118-6
Cunningham, N.J., Spencer, J.R., Feldman, P.D., Strobel, D.F., France, K., Osterman, S.N.: Detection of Callisto's oxygen atmosphere with the Hubble Space Telescope. Icarus **254**, 178–189 (2015). doi:10.1016/j.icarus.2015.03.021
Duling, S., Saur, J., Wicht, J.: Consistent boundary conditions at nonconducting surfaces of planetary bodies: applications in a new Ganymede MHD model. J. Geophys. Res. Space Phys. **119**, 4412–4440 (2014). doi:10.1002/2013JA019554
Feldman, P.D., Most, H.W., Retherford, K., Strobel, D.F., Wolven, B.C., McGrath, M.A., Roesler, F.L., Woodward, R.C., Oliversen, R.J., Ballester, G.E.: Lyman-alpha imaging of the SO_2 distribution on Io. Geophys. Res. Lett. **27**, 1787–1790 (2000)
Frank, L.A., Paterson, W.R., Khurana, K.K.: Observations of thermal plasmas in Jupiter's magnetotail. J. Geophys. Res. **107**(A1), 101029 (2002)
Goertz, C.K.: Io's interaction with the plasma torus. J. Geophys. Res. **85**(A6), 2949–2956 (1980)
Hall, D.T., Feldman, P.D., McGrath, M.A., Strobel, D.F.: The far-ultraviolet oxygen airglow of Europa and Ganymede. Astrophys. J. **499**(5), 475 (1998)
Hartkorn, O., Saur, J., Strobel, D.F.: Structure and density of Callisto's atmosphere from a fluid-kinetic model of its ionosphere: comparison with Hubble Space Telescope and Galileo observations. J. Geophys. Res. Planets **282**, 237–259 (2017). doi:10.1016/j.icarus.2016.09.020
Hill, T.W.: Inertial limit on corotation. J. Geophys. Res. **84**(A11), 6554–6558 (1979)
Hill, T.W.: The Jovian auroral oval. J. Geophys. Res. **106**(A5), 8101–8107 (2001)
Hussmann, H., Sohl, F., Spohn, T.: Subsurface oceans and deep interiors of medium-sized outer planet satellites and large trans-neptunian objects. Icarus **185**, 258–273 (2006)
Ip, W., Kopp, A.: Resistive MHD simulations of Ganymede's magnetosphere: 2. Birkeland currents and particle energetics. J. Geophys. Res. **107**, CiteID 1491 (2002)
Jia, X., Walker, R., Kivelson, M., Khurana, K., Linker, J.: Three-dimensional MHD simulations of Ganymede's magnetosphere. J. Geophys. Res. **113**, A06212 (2008)
Jia, X., Walker, R., Kivelson, M., Khurana, K., Linker, J.: Properties of Ganymede's magnetosphere inferred from improved three-dimensional MHD simulations. J. Geophys. Res. **114**, A09209 (2009). doi:10.1029/2009JA014375
Jia, X., Walker, R.J., Kivelson, M.G., Khurana, K.K., Linker, J.A.: Dynamics of Ganymede's magnetopause: intermittent reconnection under steady external conditions. J. Geophys. Res. Space Phys. **115**, A12202 (2010). doi:10.1029/2010JA015771
Joy, S.P., Kivelson, M.G., Walker, R.J., Khurana, K.K., Russell, C.T., Ogino, T.: Probabilistic models of the Jovian magnetopause and bow shock locations. J. Geophys. Res. Space Phys. **107**, 1309 (2002). doi:10.1029/2001JA009146
Khurana, K.K., Kivelson, M.G., Stevenson, D.J., Schubert, G., Russell, C.T., Walker, R.J., Polanskey, C.: Induced magnetic fields as evidence for subsurface oceans in Europa and Callisto. Nature **395**, 777–780 (1998)
Khurana, K.K., et al.: The configuration of Jupiter's magnetosphere. In: Bagenal, F. (ed.) Jupiter, chap. 24, pp. 593–616. Cambridge University Press, Cambridge (2004)
Khurana, K.K., Jia, X., Kivelson, M.G., Nimmo, F., Schubert, G., Russell, C.T.: Evidence of a global magma ocean in Io's interior. Science **332**, 1186 (2011). doi:10.1126/science.1201425
Kivelson, M.G., Khurana, K.K., Russell, C.T., Walker, R.J., Warnecke, J., Coroniti, F.V., Polanskey, C., Southwood, D.J., Schubert, G.: Discovery of Ganymede's magnetic field by the Galileo spacecraft. Nature **384**, 537–541 (1996)
Kivelson, M.G., Khurana, K.K., Joy, S., Russell, C.T., Southwood, D.J., Walker, R.J., Polanskey, C.: Europa's magnetic signature: report from Galileo's first pass on 19 December 1996. Science **276**, 1239–1241 (1997)

Kivelson, M.G., Warnecke, J., Bennett, L., Joy, S., Khurana, K.K., Linker, J.A., Russell, C.T., Walker, R.J., Polanskey, C.: Ganymede's magnetosphere: magnetometer overview. J. Geophys. Res. **103**, 19963–19972 (1998). doi:10.1029/98JE00227

Kivelson, M.G., Khurana, K.K., Russell, C.T., Volwerk, M., Walker, J., Zimmer, C.: Galileo magnetometer measurements: a stronger case for a subsurface ocean at Europa. Science **289**(5483), 1340–1343 (2000)

Kivelson, M.G., Khurana, K.K., Volwerk, M.: The permanent and inductive magnetic moments of Ganymede. Icarus **157**, 507–522 (2002)

Kivelson, M.G., Bagenal, F., Neubauer, F.M., Kurth, W., Paranicas, C., Saur, J.: Magnetospheric interactions with satellites. In: Bagenal, F., (ed.) Jupiter, chap. 21, pp. 513–536. Cambridge University Press, Cambridge (2004)

Kliore, A.J., Anabtawi, A., Herrea, R., Asmar, S., Nagy, A., Hinson, D.P., Flasar, F.M.: The ionosphere of Callisto from Galileo radio occultation observations. J. Geophys. Res. **107**, 1407 (2002). doi:10.1029/2002JA009365

Knight, S.: Parallel electric fields. Planet. Space Sci. **21**, 741 (1973)

Kopp, A., Ip, W.: Resistive MHD simulations of Ganymede's magnetosphere: 1. Time variabilities of the magnetic field topology. J. Geophys. Res. **107**, SMP 41.1, CiteID 1490 (2002)

Krupp, N., et al.: Dynamics of the Jovian Magnetosphere. In: Bagenal, F. (ed.) Jupiter, chap. 25, pp. 617–638. Cambridge University Press, Cambridge (2004)

Lanza, A.F.: Hot Jupiters and stellar magnetic activity. Astron. Astrophys. **487**, 1163–1170 (2008). doi:10.1051/0004-6361:200809753, 0805.3010

Liuzzo, L., Feyerabend, M., Simon, S., Motschmann, U.: The impact of Callisto's atmosphere on its plasma interaction with the Jovian magnetosphere. J. Geophys. Res. Space Phys. **120**, 9401–9427 (2015). doi:10.1002/2015JA021792

Liuzzo, L., Simon, S., Feyerabend, M., Motschmann, U.: Disentangling plasma interaction and induction signatures at Callisto: the Galileo C10 flyby. J. Geophys. Res. Space Phys. **121**, 8677–8694 (2016). doi:10.1002/2016JA023236

Mauk, B., Mitchell, D., Krimigis, S., Roelof, E., Paranicas, C.: Energetic neutral atoms from a trans-Europa gas torus at Jupiter. Nature **412**(6926), 920–922 (2003)

McGrath, M.A., Jia, X., Retherford, K.D., Feldman, P.D., Strobel, D.F., Saur, J.: Aurora on Ganymede. J. Geophys. Res. **118**, 2043–2054 (2013). doi:10.1002/jgra.50122

McNutt, R., Belcher, J., Bridge, H.: Positive ion observations in the middle magnetosphere of Jupiter. J. Geophys. Res. **86**, 8319–8342 (1981)

Moriguchi, T., Nakamizo, A., Tanaka, T., Obara, T., Shimazu, H.: Current systems in the Jovian magnetosphere. J. Geophys. Res. Space Phys. **113**, A05204 (2008). doi:10.1029/2007JA012751

Neubauer, F.M.: Nonlinear standing Alfvén wave current system at Io: theory. J. Geophys. Res. **85**(A3), 1171–1178 (1980)

Neubauer, F.M.: The sub-Alfvénic interaction of the Galilean satellites with the Jovian magnetosphere. J. Geophys. Res. **103**(E9), 19843–19866 (1998)

Ogino, T., Walker, R.J., Kivelson, M.G.: A global magnetohydrodynamic simulation of the Jovian magnetosphere. J. Geophys. Res. **103**, 225 (1998). doi:10.1029/97JA02247

Parker, E.N.: Dynamics of the interplanetary gas and magnetic fields. Astrophys. J. **128**, 664 (1958). doi:10.1086/146579

Paty, C., Winglee, R.: Multi-fluid simulations of Ganymede's magnetosphere. Geophys. Res. Lett. **31**, L24806 (2004)

Paty, C., Winglee, R.: The role of ion cyclotron motion at Ganymde: magnetic morphology and magnetospheric dynamics. Geophys. Res. Lett. **33**, L10106 (2006)

Paty, C., Paterson, W., Winglee, R.: Ion energization in Ganymede's magnetosphere: using multifluid simulations to interpret ion energy spectrograms. J. Geophys. Res. **113**, A06211 (2008). doi:10.1029/2007JA012848

Preusse, S., Kopp, A., Büchner, J., Motschmann, U.: A magnetic communication scenario for hot Jupiters. Astron. Astrophys. **460**, 317–322 (2006). doi:10.1051/0004-6361:20065353

Radioti, A., GéRard, J.C., Grodent, D., Bonfond, B., Krupp, N., Woch, J.: Discontinuity in Jupiter's main auroral oval. J. Geophys. Res. Space Phys. **113**, A01215 (2008). doi:10.1029/2007JA012610

Rambaux, N., van Hoolst, T., Karatekin, Ö.: Librational response of Europa, Ganymede, and Callisto with an ocean for a non-Keplerian orbit. Astron. Astrophys. **527**, A118 (2011). doi:10.1051/0004-6361/201015304

Ray, L.C., Ergun, R.E., Delamere, P.A., Bagenal, F.: Magnetosphere-ionosphere coupling at Jupiter: effect of field-aligned potentials on angular momentum transport. J. Geophys. Res. Space Phys. **115**, A09211 (2010). doi:10.1029/2010JA015423

Saur, J., Strobel, D.F., Neubauer, F.M.: Interaction of the Jovian magnetosphere with Europa: constraints on the neutral atmosphere. J. Geophys. Res. **103**(E9), 19947–19962 (1998)

Saur, J., Politano, H., Pouquet, A., Matthaeus, W.: Evidence for weak MHD turbulence in the middle magnetosphere of Jupiter. Astron. Astrophys. **386**(2), 699 (2002)

Saur, J., Strobel, D., Neubauer, F., Summers, M.: The ion mass loading rate at Io. Icarus **163**, 456–468 (2003)

Saur, J., Grambusch, T., Duling, S., Neubauer, F.M., Simon, S.: Magnetic energy fluxes in sub-Alfvénic planet star and moon planet interactions. Astron. Astrophys. **552**, A119 (2013). doi:10.1051/0004-6361/201118179

Saur, J., Duling, S., Roth, L., Jia, X., Strobel, D.F., Feldman, P.D., Christensen, U.R., Retherford, K.D., McGrath, M.A., Musacchio, F., Wennmacher, A., Neubauer, F.M., Simon, S., Hartkorn, O.: The search for a subsurface ocean in Ganymede with Hubble Space Telescope observations of its auroral ovals. J. Geophys. Res. Space Phys. **120**, 1715–1737 (2015). doi:10.1002/2014JA020778

Seufert, M.: Callisto: induction signals, atmosphere and plasma interaction. Dissertation, Institut für Geophysik und Meteorologie der Universität zu Köln (2012)

Seufert, M., Saur, J., Neubauer, F.M.: Multi-frequency electromagnetic sounding of the Galilean moons. Icarus **214**, 477–494 (2011). doi:10.1016/j.icarus.2011.03.017

Showman, A.P., Malhotra, R.: The Galilean satellites. Science **296**, 77–84 (1999)

Sohl, F., Spohn, T., Breuer, D., Nagel, K.: Implications from Galileo observations on the interior structure and chemistry of the Galilean satellites. Icarus **157**, 104–119 (2002)

Southwood, D.J., Kivelson, M.G.: A new perspective concerning the influence of the solar wind on the Jovian magnetosphere. J. Geophys. Res. **106**, 6123–6130 (2001). doi:10.1029/2000JA000236

Southwood, D.J., Kivelson, M.G., Walker, R.J., Slavin, J.A.: Io and its plasma environment. J. Geophys. Res. **85**(A11), 5959–5968 (1980)

Strobel, D.F., Saur, J., Feldman, P.D., McGrath, M.A.: Hubble Space Telecope Space Telescope Imaging Spectrograph search for an atmosphere on Callisto: a Jovian unipolar inductor. Astrophys. J. Lett. **581**, L51–L54 (2002)

Vance, S., Bouffard, M., Choukroun, M., Sotin, C.: Ganymede's internal structure including thermodynamics of magnesium sulfate oceans in contact with ice. Planet. Space Sci. **96**, 62–70 (2014). doi:10.1016/j.pss.2014.03.011

Vasyliūnas, V.M.: Plasma distribution and flow. In: Dessler, A.J. (ed.) Physics of the Jovian Magnetosphere, chap. 11, pp. 395–453. Cambridge University Press, Cambridge (1983)

Vogt, M.F., Jackman, C.M., Slavin, J.A., Bunce, E.J., Cowley, S.W.H., Kivelson, M.G., Khurana, K.K.: Structure and statistical properties of plasmoids in Jupiter's magnetotail. J. Geophys. Res. Space Phys. **119**, 821–843 (2014). doi:10.1002/2013JA019393

Walker, R.J., Ogino, T.: A simulation study of currents in the Jovian magnetosphere. Planet. Space Sci. **51**, 295–307 (2003). doi:10.1016/S0032-0633(03)00018-7

Zimmer, C., Khurana, K., Kivelson, M.: Subsurface oceans on Europa and Callisto: constraints from Galileo magnetometer observations. Icarus **147**, 329–347 (2000)